

Improved interface quality and luminescence capability of InGaN/GaN quantum wells with Mg pretreatment

Zhengyuan Wu¹ · Xiyang Shen¹ · Huan Xiong¹ · Qingfei Li¹ · Junyong Kang¹ · Zhilai Fang¹ · Feng Lin² · Bilan Yang² · Shilin Lin² · Wenzhong Shen³ · Tong-Yi Zhang⁴

Received: 8 July 2015 / Accepted: 21 January 2016 / Published online: 1 February 2016
© Springer-Verlag Berlin Heidelberg 2016

Abstract Interface modification of high indium content InGaN/GaN quantum wells was carried out by Mg pretreatment of the GaN barrier surface. The indium in the Mg-pretreated InGaN layer was homogeneously distributed, making the interfaces abrupt. The improved interface quality greatly enhanced light emission capacity. The cathodoluminescence intensity of the Mg-pretreated InGaN/GaN quantum wells was correspondingly much stronger than those of the InGaN/GaN quantum wells without Mg pretreatment.

1 Introduction

While the group III nitrides have been intensively studied and successfully applied in fabrication of electronic and optoelectronic devices [1–5], the epitaxial growth of high-quality and high indium content InGaN layers for high brightness and reliable devices applications is still a big

challenge [6–12]. This is because high-density threading dislocations (TDs) and point defects usually exist in the high indium content InGaN layer and/or at the interface when the InGaN layer is epitaxially deposited on a GaN layer due to the large lattice mismatch between the two crystalline layers. These defects increase nonradiative recombination rate and may damage the device. In addition, the intrinsic internal electric field and strong strain-induced piezoelectric polarization field in the active layer, which cause a local separation of electrons and holes within the active regions, result in significant reduction in radiative recombination rate. Increasing indium content in the InGaN layer increases the lattice mismatch and deteriorates the crystalline quality further. Consequently, the quantum-confined Stark effect (QCSE) becomes more severe, leading to a significant drop of internal quantum efficiency (IQE) [13–16]. To overcome the problems, one may grow thin InGaN active layer to enhance the overlap of electron and hole wave functions and thus increase the IQE. By decreasing the thickness of high indium content InGaN layer, the strain relaxation by defect formation, which would increase the nonradiative recombination rate, would be suppressed. The epitaxy of high indium content InGaN layer with low TDs density and especially with atomically smooth and sharp interfaces and homogenous indium distribution has become critical for high indium content InGaN/GaN-based devices [17, 18].

The surface structures and properties of a layer (or substrate) play a critical role in the subsequent epitaxial growth behavior. Surface treatment has been successfully applied to improve the surface (or interface after deposited a top layer) qualities, growth behavior, and device performance [19–27]. For instance, the surface modification of GaN films by gallium droplet epitaxy successfully improved the crystalline quality and optical properties of

✉ Zhilai Fang
zhilai.fang@hotmail.com

Tong-Yi Zhang
zhangty@shu.edu.cn

¹ Collaborative Innovation Center for Optoelectronic Semiconductors and Efficient Devices, Department of Physics, Xiamen University, Xiamen 361005, China

² San'an Optoelectronics Co., Ltd, Xiamen 361009, China

³ Key Laboratory of Artificial Structures and Quantum Control (Ministry of Education), Department of Physics, Shanghai Jiao Tong University, Shanghai 200240, China

⁴ Shanghai University Materials Genome Institute and Shanghai Materials Genome Institute, Shanghai University, 99 Shangda Road, Shanghai 200444, China

the subsequently grown InGaN layer [23, 24]. The defect density of GaN films was substantially reduced by inserting a very thin heavily Mg-doped GaN layer [25]. Appropriate Mg doping in InGaN layer improved the surface smoothness and reduced the polarization field [26]. Enhanced hole injection was achieved by Mg doping in the GaN barriers [27].

In this study, Mg pretreatment of the GaN barrier surface was carried out prior to the epitaxial growth of the InGaN active layer. The Mg pretreatment was expected to modify the growth behavior of the InGaN/GaN quantum wells (QWs). For instance, indium incorporation behavior will be modified, especially around the dislocation pits where Mg atoms would be most likely present. We found that the Mg pretreatment greatly improved the quality of the InGaN layer with homogeneous indium distribution and an abrupt interface between the underneath GaN layer, thereby considerably enhancing blue–green light emission.

2 Growth, characterization, and simulation

2.1 Epitaxy

The metalorganic vapor phase epitaxy (MOVPE) of GaN films, InGaN QWs, and GaN barriers was carried out on c-sapphire substrates. Trimethylgallium (TMGa), Trimethylindium (TMIn), and high-purity ammonia were used as the source precursors. During the growth of InGaN QWs and GaN barriers, nitrogen was used as the carrier gas, whereas hydrogen was used as the carrier gas in the other growth stages.

Figure 1 shows the schematic diagram of the growth structure of the InGaN/GaN QWs without and with the Mg pretreatment. The sapphire substrates were cleaned at 1060 °C and 100 Torr for 15 min in H₂ ambient followed by nitridation at 550 °C for 4 min. A conventional 25-nm low-temperature GaN nucleation layer was grown at 535 °C and 500 Torr followed by annealing at 1035 °C for 10 min [28]. The subsequent growth of high-temperature (HT) GaN film (~2.0 μm) was carried out at

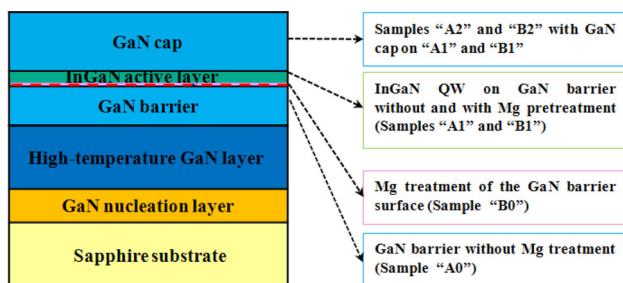


Fig. 1 Schematic diagram of the InGaN/GaN SQW structure

1035 °C and 100 Torr with TMGa/NH₃ ratio gradually increasing from 970 to 2450. For sample “A0,” the bottom GaN barrier was grown on the HT GaN film at 786 °C and 300 Torr. For sample “B0,” additional Mg treatment was performed to sample “A0” by a biscyclopentadienyl magnesium (Cp₂Mg) flow (60 sccm) over the GaN barrier surface for 12 s (called Mg treatment process). A chart is shown in Fig. 2 to illustrate the growth conditions (growth temperature and time, TMIn, TMGa, and Cp₂Mg) of the Mg-pretreated InGaN/GaN QW. Except for the Mg treatment process, the other growth conditions for the InGaN/GaN QWs remained the same for the untreated and Mg-pretreated samples. As shown in Fig. 2, the untreated and Mg-pretreated GaN barriers were annealed at 786 °C for 15 s and then cooled down to 670 °C in 300 s, which was called the cooling process, for the subsequent growth of InGaN layer on both samples “A1” and “B1.” In order to suppress the strain relaxation-induced defect formation and the QCSE, which were usually observed for the relatively “thick” (>2.5 nm) high indium content (>25 %) InGaN layer grown at low temperature [29, 30], relatively thin InGaN active layer was grown in this study. For samples “A2” and “B2,” a GaN cap was subsequently grown on samples “A1” and “B1” at 786 °C. Before temperature ramping for the growth of GaN cap, a very thin GaN layer was grown at 670 °C to suppress the indium desorption and outdiffusion [7, 31]. The InGaN/GaN single-QW (SQW) samples were prepared for the study of interface modification on growth dynamics and luminescence mechanism. Five-period InGaN/GaN multiple-QWs (MQWs) samples were also prepared for X-ray diffraction (XRD) investigation.

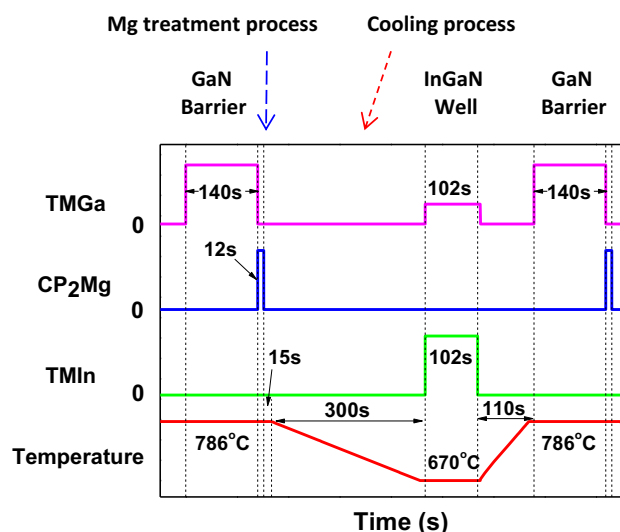


Fig. 2 A chart of the growth conditions (growth temperature and time, TMIn, TMGa, and Cp₂Mg) of the first InGaN/GaN QW

2.2 Characterization

The surface morphologies of the GaN and InGaN layer were investigated by atomic force microscopy (AFM, SPA400, Seiko Instruments Inc.). The surface chemical compositions were analyzed by X-ray photoelectron spectroscopy (XPS, Kratos AXIS Ultra DLD) with an Al K_{α} X-ray excitation source ($h\nu = 1486.6$ eV). High-resolution XRD (HR-XRD, PANalytical X'pert-Pro) was used to analyze the interface quality, average indium content, and period thickness of the Mg-pretreated InGaN/GaN MQWs. A scanning electron microscope (SEM, Sirion200) combined with cathodoluminescence (CL, Gatan MonoCL3+) was employed to characterize the spatially resolved luminescence properties with relatively high carrier injection. The microstructures of the InGaN/GaN QWs were investigated by high-resolution high-angle annular dark field scanning transmission electron microscopy (HAADF-STEM, Tecnai G2 F20 S-TWIN).

2.3 Simulation

Crosslight's APSYS software was employed to simulate the physical parameters of the InGaN/GaN QWs [32]. The APSYS is based on 2D/3D finite element analysis of electrical, optical, and thermal properties of compound semiconductor devices. The energy band structures and luminescence properties were numerically studied. In numerical simulations, the simulator solves Schrödinger–Poisson equations self-consistently. The polarization screening factor is set to 0.5. The other parameters used in the simulations can be found elsewhere [32].

3 Results and discussion

3.1 Modification in growth behavior and growth dynamics: surface morphology and composition analysis

Figure 3a, b shows the AFM images of samples “A0” and “B0,” respectively. The surfaces are of layer structure with surface pits emerging at the terrace edges with a pit density of about 3.6×10^8 for both samples. Obviously, the pit size in sample “B0” is generally bigger than that in sample “A0.” As an example, Fig. 3c shows the inverted pyramid shape and the pit size and depth along lines L1 and L2 marked on the images of Fig. 3a, b, respectively, for samples “A0” and “B0.” Figure 3d shows the XPS spectra of the Mg 2p photoelectron peaks for samples “A0” and “B0,” indicating about 1.8 at.% Mg atomic concentration in the Mg-pretreated sample “B0.” The Mg atoms might be most likely present at the pit sites [33], which increase the

average pit size from ~ 120 to ~ 180 nm and average pit depth from ~ 1.2 to ~ 1.6 nm, as shown in Fig. 3c.

Figure 4a shows the surface morphology of sample “A1,” i.e., with bare InGaN layers on sample “A0.” The estimated pit density, average pit size, and depth are about 6.0×10^8 cm^{-2} , 250 and 2.5 nm, respectively. With Mg pretreatment for sample “B1,” the surface morphology in Fig. 4b changes drastically and is featured by interlinked InGaN layer with shallow troughs (~ 1.3 nm in depth) between them. As schematically shown in Fig. 4c, the trough formation is most likely caused by the preferential aggregation of Mg around the dislocation pits, which prevents the further nucleation of InGaN around the pit arrays and results in the formation of InGaN-deficient troughs [34, 35]. Less indium incorporation around the dislocation pits would form relatively high surface potential around the dislocation pit arrays and thus may suppress carrier transport to the dislocation cores.

Figure 5 shows the XPS spectra (after background subtraction and intensity normalization to the Ga 2p₃ peak) of the Ga 2p₃ and In 3d₅ photoelectron peaks from samples “A1” and “B1.” The indium content can be estimated by $X_{\text{In}} = \frac{I_{\text{In } 3d_5} / F_{\text{In } 3d_5}}{I_{\text{In } 3d_5} / F_{\text{In } 3d_5} + I_{\text{Ga } 2p_3} / F_{\text{Ga } 2p_3}}$, where I denotes the integrated intensity of the XPS photoelectron peaks and F the sensitivity factors ($F_{\text{Ga } 2p_3} = 2.75$ and $F_{\text{In } 3d_5} = 4.53$) [36]. The average indium content in the InGaN layer is roughly estimated as about 41 % for the untreated sample “A1,” while it is about 38 % for the Mg-pretreated sample “B1.” As shown in Fig. 5b, c, the full width at half maximum (FWHM) of the In 3d₅ peak is 1.64 eV for sample “A1” and 1.50 eV for sample “B1.” The In 3d₅ photoelectron peak is composed of two components corresponding to the chemical bonding of In–N (~ 444.2 eV) and In–O (~ 444.9 eV) due to the oxidation of indium [37, 38]. The fitted In 3d₅ (In–O) peak intensity from sample “B1” is much lower than that from sample “A1,” leading to the narrowing of the FWHM of the In 3d₅ peak from sample “B1.” A low In–O peak is caused by one of the two factors: less chemically active In atoms and less available oxygen. The basically same fabrication process for samples “A1” and “B1” means the same oxidation environment for the two samples. Thus, the fact that the In–O peak in sample “B1” is lower than that in sample “A1” might indicate that the chemically active In atoms in sample “B1” is less than that in sample “A1.” Usually, In-rich nanostructures contain more chemically active In atoms, which are keen to oxidation. The experimental result might imply that In-rich nanostructures were formed in sample “A1” and likely suppressed in sample “B1.” The presence of Mg atoms on the surface may also suppress the formation of indium oxide. As indium incorporation is impeded by the Mg aggregation around the arrays of the chemically active dislocation pits [34, 35], the slight

Fig. 3 AFM images of samples **a** “A0” and **b** “B0.” **c** Typical line profiles “L1” and “L2” crossing over the surface pits on the samples “A0” and “B0,” respectively. **d** XPS spectra of the Mg 2p photoelectron peaks from samples “A0” and “B0”

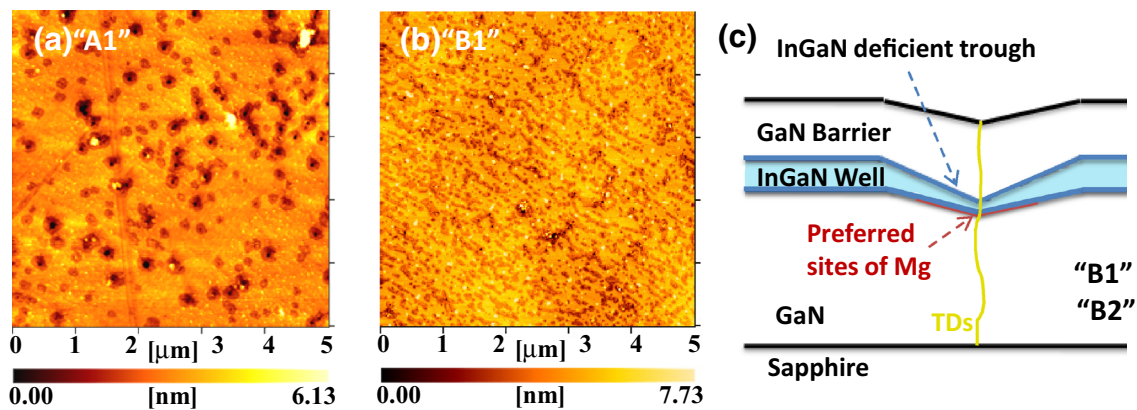
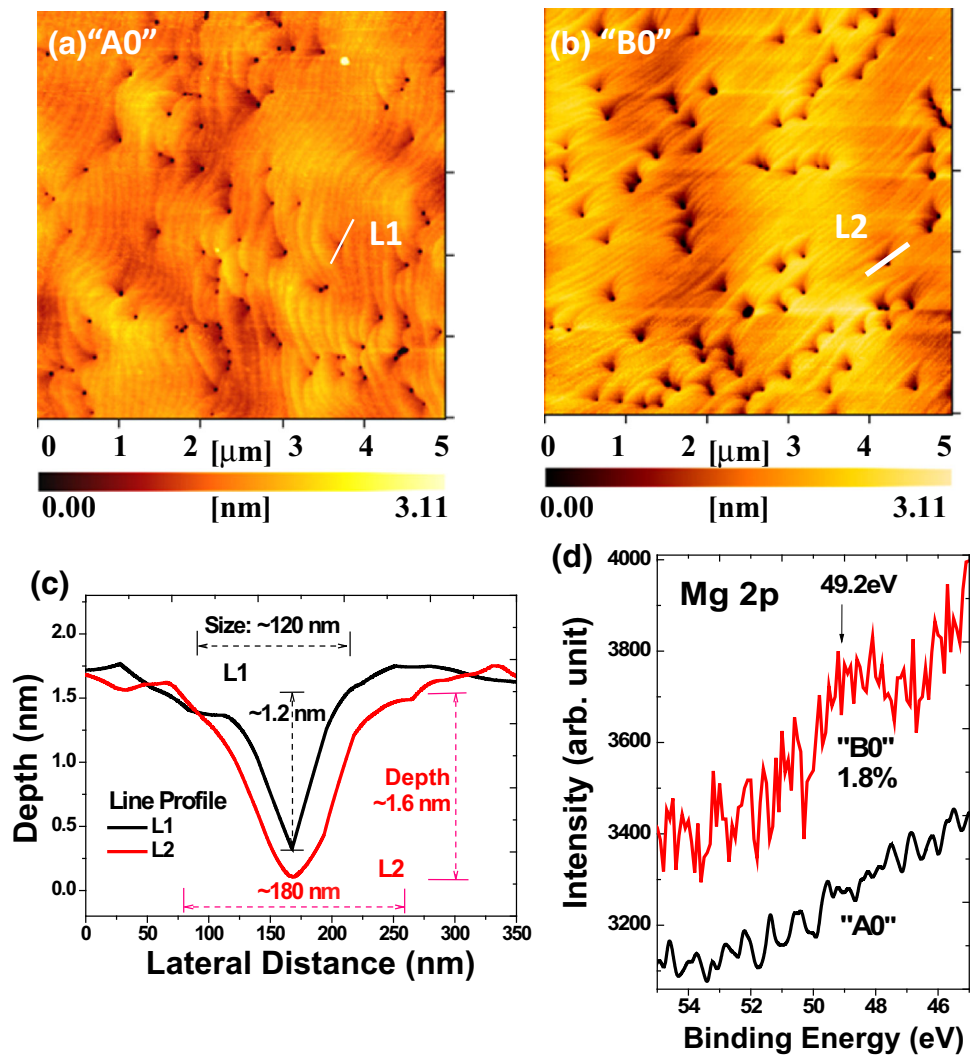


Fig. 4 AFM images of samples **a** “A1” and **b** “B1.” **c** Schematic diagram of the formation of InGaN-deficient troughs

decrease in average indium content within the InGaN layer for sample “B1” is consistent with the formation of InGaN-deficient troughs around the pit arrays. Both changes in surface morphology and indium content are correlated with the Mg pretreatment of the bottom GaN layers. Moreover, the

suppression of the In-rich nanostructures formation may also be responsible for the decrease in average indium content in the Mg-pretreated sample “B1.”

Samples “A2” and “B2” were obtained by growth of GaN cap on samples “A1” and “B1,” respectively. As

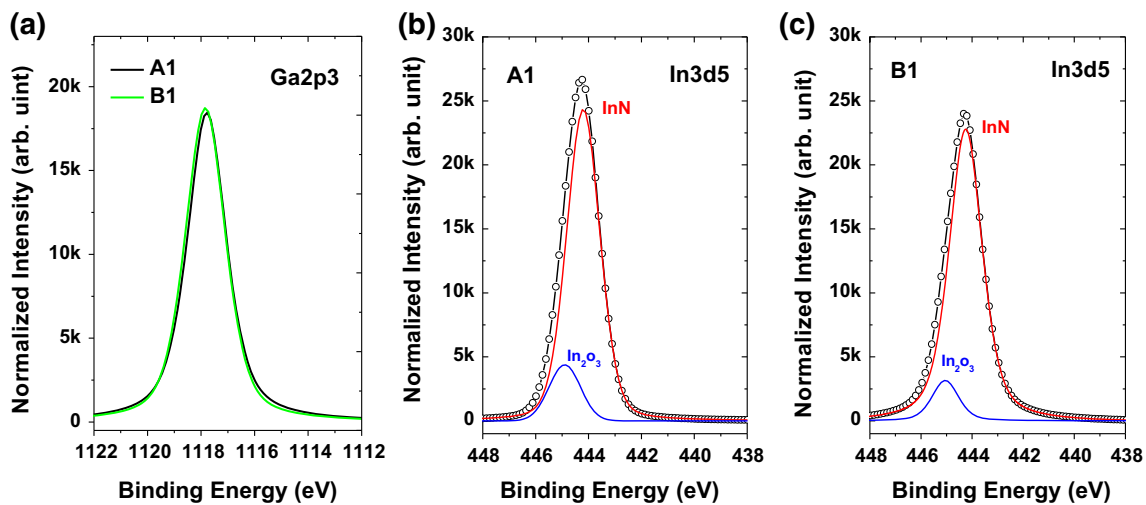


Fig. 5 XPS spectra of samples “A1” and “B1”: **a** the normalized Ga 2p3 photoelectron peak and the In 3d5 photoelectron peaks of **b** sample “A1” and **c** sample “B1.” The In 3d5 photoelectron peak is

composed of two components corresponding to the chemical bonding of In–N and In–O

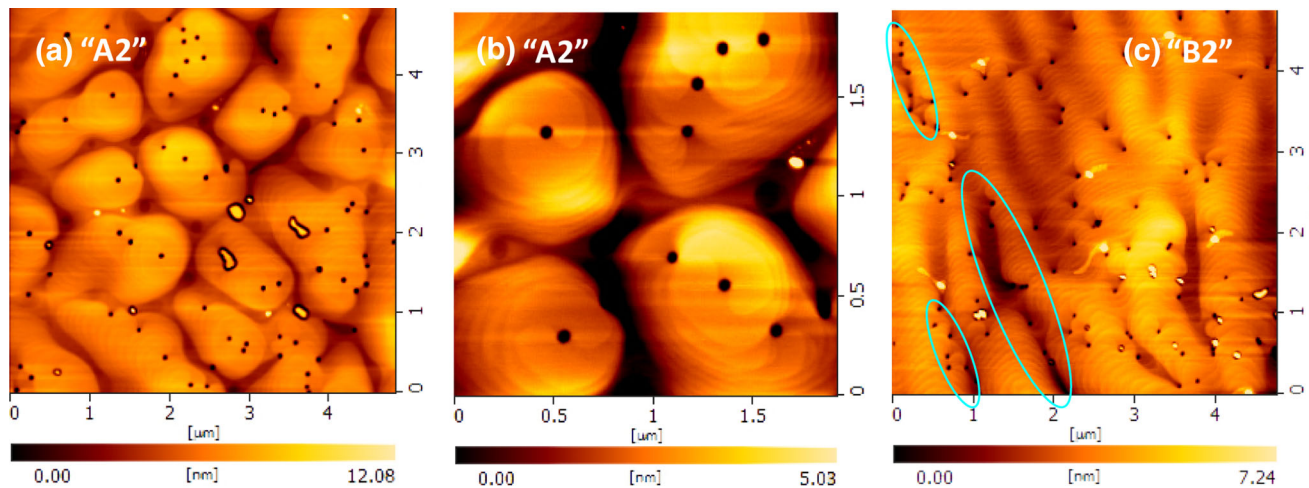


Fig. 6 AFM images of samples “A2” and “B2”: **a** “A2,” $5 \times 5 \mu\text{m}^2$, **b** “A2,” $2 \times 2 \mu\text{m}^2$, and **c** “B2,” $5 \times 5 \mu\text{m}^2$

shown in Fig. 6a, the surface of sample “A2” is rough with an rms roughness of about 1.6 nm. The average pit size, depth, and density are about 86 nm, 12 nm, and $3.7 \times 10^8 \text{ cm}^{-2}$, respectively. The reduction in pit density in sample “A2” compared with that in sample “A1” is likely due to the enhanced adatom diffusion during the growth of GaN capping layers at relatively high temperature and the TDs termination at the InGaN-to-GaN interface (dislocation bending at the heterogeneous interfaces) [39–41]. The surface is characterized by lots of dislocation pits and spiral mounds, which were formed by step pinning followed by spiral growth of the GaN capping layers around the dislocation cores. In Fig. 6b for the enlarged view of the surface mounds, high-density pinned steps and

various growth spirals are clearly visible. The pinned surface steps wind themselves around the dislocation cores and evolve into spirals and spiral mounds. Some neighboring spiral mounds coalesce and form one hillock with several pits on it. The spiral growth instead of layer growth during the subsequent growth of GaN barrier on the high indium content ($\sim 41\%$) InGaN layer is due to stabilization of the spiral growth by reduction in attachment of Ga adatoms to the In-rich dislocation cores (otherwise, the growth spirals would be annihilated) [42]. Accordingly, as shown in Fig. 6a, b, discrete large spiral mounds grow and eventually coalesce. Spiral growth, usually correlating with an increase in indium content in the center of the spiral domains (dislocation cores) in comparison with their

periphery [43], would enhance carrier trapping at the TDs sites and thus increase the nonradiative recombination rate.

Figure 6c shows the surface morphology of sample “B2” with a GaN cap on sample “B1,” exhibiting homogeneous and straight pinned steps on the surface. The emergence of shallow troughs with pit arrays mainly aligning the troughs (e.g., the circled area) is a consequence of the surface structures of the bottom layers featured by arrays of pits (sample “B0,” Fig. 3b) and shallow troughs (sample “B1,” Fig. 4b). Away from the troughs, the surface layer structure is distinct, indicating layer growth of the GaN cap. The surface is relatively smooth with an rms roughness of about 1.0 nm. The average pit size, depth, and density are about 70, 5.0 nm, and $3.8 \times 10^8 \text{ cm}^{-2}$, respectively. Considering that spiral growth is detrimental to optoelectronic devices, the Mg pretreatment technique employed in this study may be an alternative to suppress the spiral growth and enhance the IQE of high indium content InGaN-based structures.

3.2 Microstructure analysis

Figure 7a shows the cross-sectional HAADF-STEM image of sample “A2.” Due to the higher atomic mass of indium compared with that of gallium, the InGaN layer has a higher intensity and thus depicted brighter than the GaN layer. Accordingly, the narrow bright contrast stripes correspond to the InGaN QW, whereas the wide dark contrast stripes correspond to the GaN barrier. The appearance of relatively bright (red circled) and dark contrasts in the InGaN QW of sample “A2” indicates the lateral fluctuation of indium content and QW thickness, and formation of In-rich regions. To further investigate the indium concentration profile of the InGaN layer along the growth direction, HR-STEM of the InGaN/GaN QW was characterized and shown in Fig. 7b. Atomic rows of GaN barrier and InGaN QW were observed for sample “A2.” The InGaN QW is 4 atomic layers thick (1.04 nm). A typical line profile crossing over the InGaN QW along the growth direction is drawn and shown Fig. 7c. To evaluate the distribution of indium content in the InGaN QW, we assume the HAADF-STEM intensity of the GaN barrier (where the indium content is zero) as the background signal and the calibrated HAADF-STEM intensity (calibration by subtraction of the background signal) linearly dependent on the indium content [9]. Considering the average indium content 41 % for the InGaN QW of sample “A2,” the HAADF-STEM intensity (left axis) in Fig. 7c can be converted to the estimated indium content (right axis). The indium concentration line profile gives the details of the interfaces, and apparently the upper InGaN-to-GaN interface shows a shoulder with a gradual decrease in indium content.

Figure 7d shows the cross-sectional HAADF-STEM image of sample “B2.” Different from sample “A2,” the InGaN QW of sample “B2” is of homogeneous indium distribution and uniform QW thickness. The GaN–InGaN–GaN interfaces in Fig. 7e are quite abrupt, and the InGaN QW is 5 atomic layers thick (1.30 nm). The line profile in Fig. 7f details the GaN–InGaN–GaN interfaces of sample “B2” and gives the indium concentration profile. Relatively abrupt GaN-to-InGaN interface (lower) and InGaN-to-GaN interface (upper) were observed with an average indium content of about 38 % within the InGaN QW. For thin InGaN QWs, the fluctuation of indium content and variation in QW thickness would greatly influence the interband transition energies and luminescence properties. Abrupt interfaces and homogeneous indium distribution are highly desirable for thin InGaN QWs emitting in the blue–green spectral region [17, 18]. Without Mg pretreatment for sample “A2,” the surface was characterized by lots of dislocation pits and spiral mounds (Fig. 6). Fluctuation of indium content and QW thickness, and generation of defects around the In-rich regions were observed (Fig. 7). In comparison, the InGaN QW of sample “B2” was of abrupt interfaces and homogeneous indium distribution, and lack of phase separation and defect generation, suggesting improvement in interface quality of the InGaN layer by the Mg pretreatment.

Figure 8 shows the HR-XRD ω - 2θ scan profile of the (0002) reflection of the Mg-pretreated InGaN/GaN MQWs. Well-resolved high-order satellite peaks were observed indicating high-quality interfaces between GaN barriers and InGaN QWs. Theoretical fitting of the spectrum by the PANalytical Epitaxy 4.3a software shows an estimated QW thickness of about 1.30 nm and average indium content of about 38 %, which are consistent with the XPS and STEM results.

3.3 Luminescence properties: the Mg pretreatment effect

Figure 9a shows the PL spectra of samples “A2” and “B2.” Distinct emission at about 465 nm (2.67 eV) from sample “A2” and much stronger emission at about 486 nm (2.55 eV) from sample “B2” were observed. Figure 9b shows the CL spectra of samples “A2” and “B2.” The CL emission peaks at about 460 nm (2.70 eV) for sample “A2” and at 485 nm (2.56 eV) for sample “B2,” respectively. The CL peak intensity of about 16,000 from sample “B2” is much higher than that of about 9600 from sample “A2.” The full width at half maximum of the CL peaks is about 27 nm for both samples. As shown in Fig. 7, the Mg pretreatment in sample “B2” slightly decreased the indium content within the InGaN QW, increased the QW thickness, and improved the interface quality (abrupt interfaces,

Fig. 7 **a** Cross-sectional HAADF-STEM image and **b** HR-STEM image showing the microstructure of the InGaN layer of sample “A2.” The red circled bright spots indicate fluctuation of indium content and formation of In-rich regions. **c** A line profile showing the indium distribution of sample “A2” along the growth direction. **d** Cross-sectional HAADF-STEM image and **e** HR-STEM image of the InGaN layer of sample “B2.” Features such as distinct interface abruptness and homogeneous indium distribution are evident. **f** A line profile showing the indium distribution of sample “B2” along the growth direction

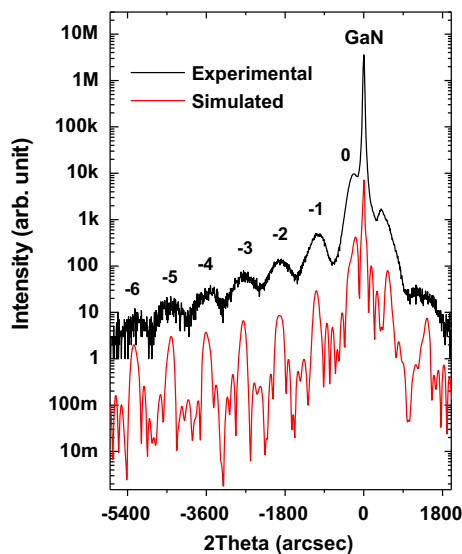
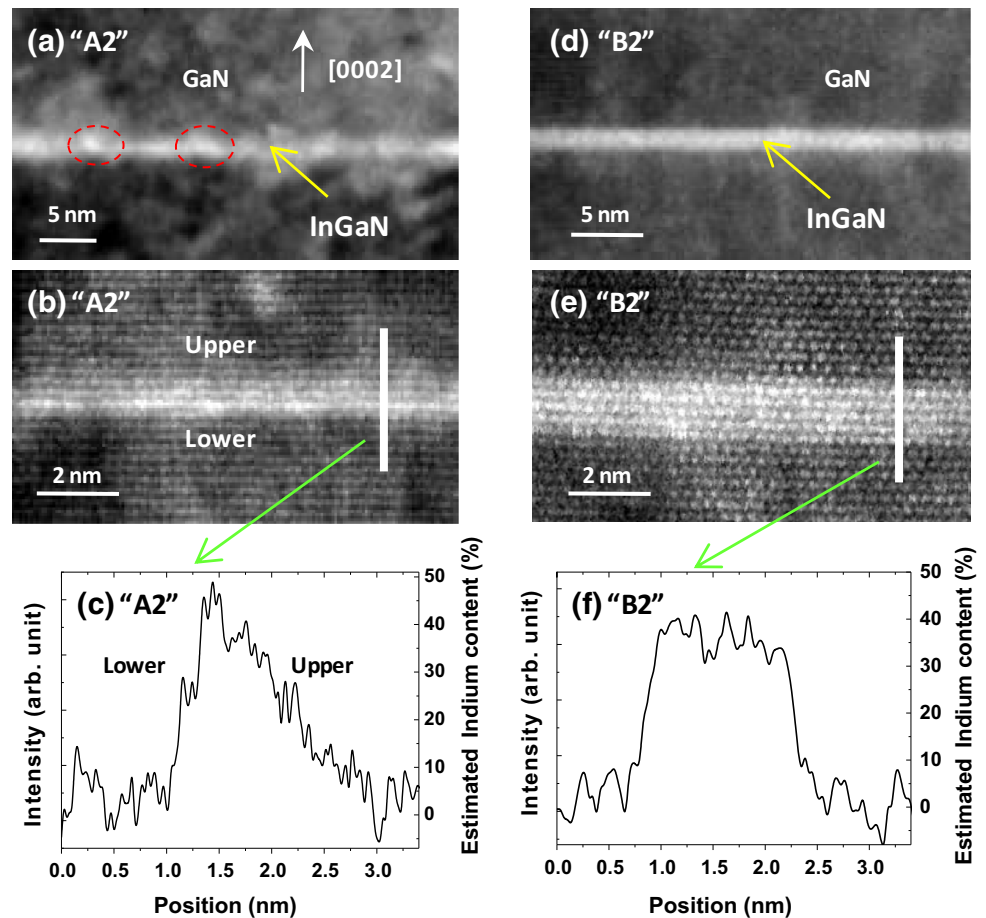


Fig. 8 Experimental and simulated XRD ω - 2θ scan profile of the (0002) reflection of the Mg-pretreated InGaN/GaN MQWs

homogeneous indium distribution, and lack of defect formation) in comparison with sample “A2” without the Mg pretreatment, even so the other process conditions for the

two samples were all the same. Additionally, less indium incorporation around the dislocation pits caused by the Mg aggregation there would form relatively high surface potential around the dislocation arrays and thus suppress carrier transport to the dislocation cores [34, 35]. These Mg pretreatment-induced changes (interface quality, indium content, QW thickness, etc.) greatly enhanced the light emission intensity from the Mg-pretreated InGaN/GaN QW. The origin of the light emission enhancement will be further studied by fabrication and comparisons of the Mg-pretreated and Mg-untreated InGaN/GaN QW LEDs with similar QW structures in the future. Figure 10 shows the surface morphology and monochromatic CL images of samples “A2” and “B2.” Relatively uniform blue–green light emission was observed for sample “B2” whereas weak and nonuniform blue light emission was observed for sample “A2,” which is also correlated with the microstructures (interface quality and indium distribution) and consistent with the PL results.

To further explore the origin of the emission spectra, APSYS was employed to simulate the physical parameters of the InGaN/GaN QWs. Based on the XPS, STEM, and XRD results, the 1.04 nm $\text{In}_x\text{Ga}_{1-x}\text{N}$ and 1.30 nm

Fig. 9 **a** PL and **b** CL spectra of samples “A2” and “B2”

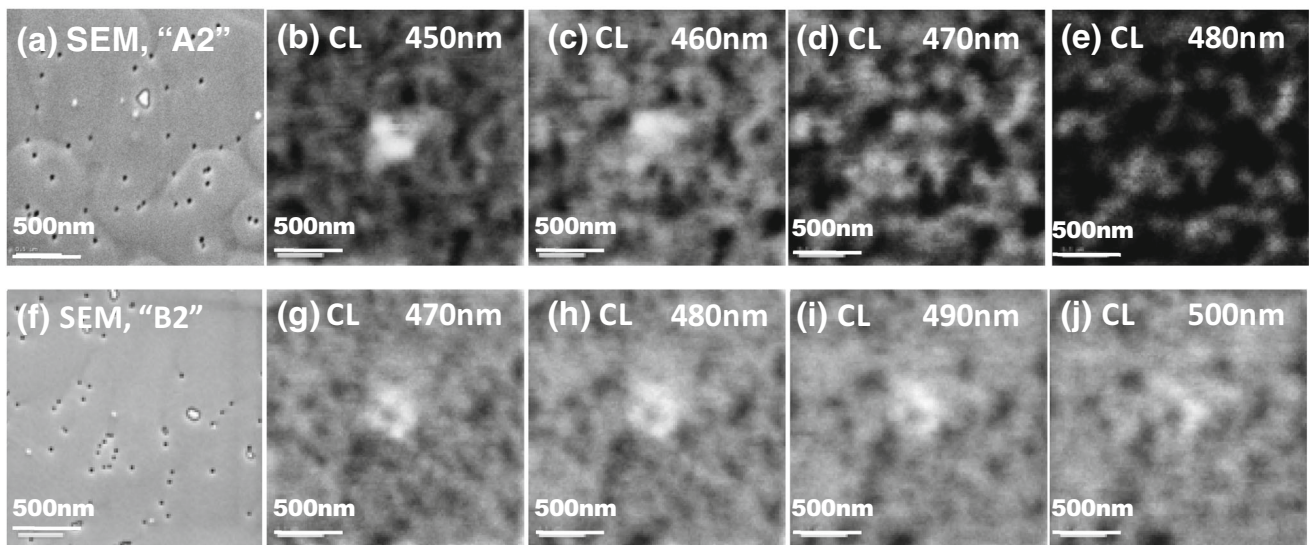
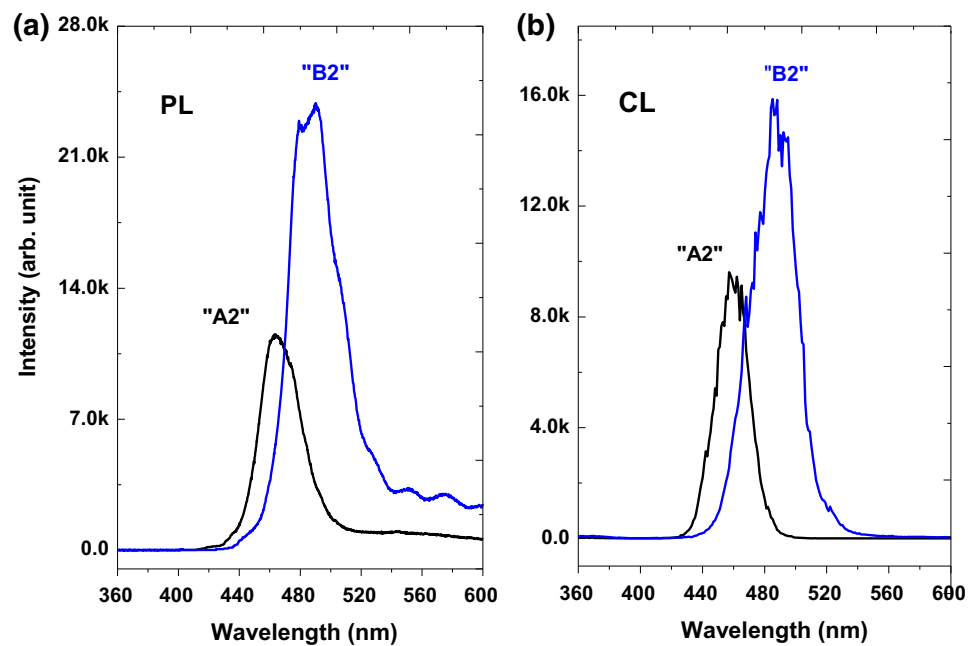


Fig. 10 aSEM image of sample “A2” and the monochromatic CL images obtained at **b** 450, **c** 460, **d** 470, and **e** 480 nm. **f** SEM image of sample “B2” and the monochromatic CL images obtained at **g** 470, **h** 480, **i** 490, and **j** 500 nm

$\text{In}_y\text{Ga}_{1-y}\text{N}$ QWs with various indium contents from 35 to 45 % have been simulated. Figure 11a shows the energy band diagram and wave functions of the 1.04 nm $\text{In}_{0.39}\text{Ga}_{0.61}\text{N}/12$ nm GaN QW structure. The interband transition energy is 2.67 eV (465 nm), which is close to the emission peak energy of sample “A2.” Figure 11b shows the energy band diagram and wave functions of the 1.30 nm $\text{In}_{0.38}\text{Ga}_{0.62}\text{N}/12$ nm GaN QW structure for sample “B2.” The interband transition energy is 2.55 eV (486 nm), which is also close to the emission peak energy

of sample “B2.” In the case of one-dimensional infinitely deep square QW, the energy levels can be easily calculated analytically. The energy difference between the conduction band minima and the subband energy level can be given by $\Delta E_n = \frac{n^2 \pi^2 \hbar^2}{2m^* L_w^2}$, where n is the quantum number, m^* the effective mass, and L_w the QW thickness. Due to the increase in QW thickness from 1.04 nm for sample “A2” to 1.30 nm for sample “B2,” the rise of subband energy level from the conduction band minima decreased, leading to the “redshift” of the emission peak of sample “B2.”

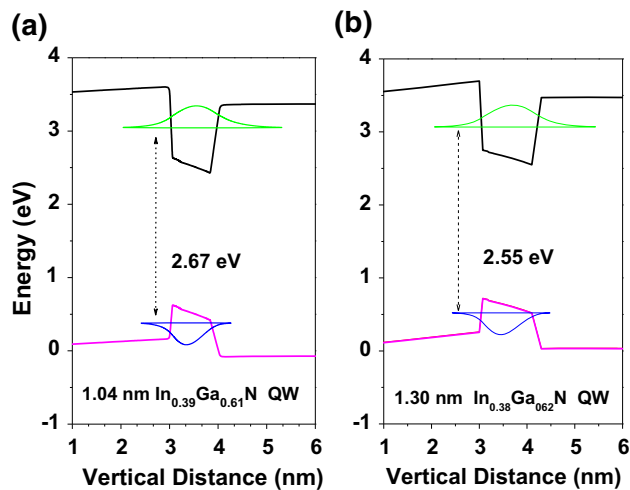


Fig. 11 Energy band structures and wave functions of **a** the 1.04 nm $\text{In}_{0.39}\text{Ga}_{0.61}\text{N}/12$ nm GaN QWs without pretreatment and **b** the 1.30 nm $\text{In}_{0.38}\text{Ga}_{0.62}\text{N}/12$ nm GaN QWs with the Mg pretreatment

4 Conclusion

In summary, by Mg pretreatment of the bottom GaN barrier surface, the growth behavior of the high indium content InGaN/GaN QWs changed greatly; the interface quality and luminescence capability were significantly improved. Without Mg pretreatment, spiral growth dominated; lateral fluctuation of indium content and QW thickness, lack of interface abruptness, and formation of In-rich regions were evident within the InGaN layer. With Mg pretreatment, the InGaN layer was of homogeneous indium distribution and abrupt interfaces as investigated by XRD and STEM. The luminescence properties were investigated by CL and further analyzed by energy band structures of various $\text{In}_x\text{Ga}_{1-x}\text{N}/\text{GaN}$ QWs. Enhanced light emission from the Mg-pretreated InGaN layer was achieved and attributed to the improvement in interface quality and suppression of non-radiative recombination at dislocation pits.

Acknowledgments This work was supported by the National Natural Science Foundation of China under Grant Nos. 60876008, 61076091, and 11544008, Program for New Century Excellent Talents in Fujian University, and the Fundamental Research Funds for the Central Universities under Grant No. 2012121008.

References

1. E.F. Schubert, J.K. Kim, *Science* **308**, 1274 (2005)
2. E.F. Schubert, J.K. Kim, H. Luo, J.Q. Xi, *Rep. Prog. Phys.* **69**, 3069 (2006)
3. B. Monemar, G. Pozina, *Prog. Quantum Electron.* **24**, 239 (2000)
4. S.P. Denbaars, D. Feezell, K. Kelchner, S. Pimputkar, C.C. Pan, C.C. Yen, S. Tanaka, Y.J. Zhao, N. Pfaff, R. Farrell, M. Iza, S. Keller, U. Mishra, J.S. Speck, S. Nakamura, *Acta Mater.* **61**, 945 (2013)

5. G.Q. Li, W.L. Wang, W.J. Yang, H.Y. Wang, *Surf. Sci. Rep.* **70**, 380 (2015)
6. N. Okada, Y. Yamada, K. Tadatomo, *J. Appl. Phys.* **111**, 043508 (2012)
7. J.W. Ju, H.S. Kim, L.W. Jang, J.H. Baek, D.C. Shin, I.H. Lee, *Nanotechnology* **18**, 295402 (2007)
8. C.F. Huang, T.Y. Tang, J.J. Huang, W.Y. Shiao, C.C. Yang, C.W. Hsu, L.C. Chen, *Appl. Phys. Lett.* **89**, 051913 (2006)
9. Y.X. Lin, Z.L. Fang, *Appl. Phys. A* **103**, 317 (2011)
10. S. De, A. Layek, S. Bhattacharya, D.K. Das, A. Kadir, A. Bhattacharya, S. Dhar, A. Chowdhury, *Appl. Phys. Lett.* **101**, 121919 (2012)
11. Z.L. Fang, Q.F. Li, X.Y. Shen, H. Xiong, J.F. Cai, J.Y. Kang, W.Z. Shen, *J. Appl. Phys.* **115**, 043514 (2014)
12. Z.L. Wu, P. Chen, G.F. Yang, Z. Xu, F. Xu, F.L. Jiang, R. Zhang, Y.D. Zheng, *Appl. Surf. Sci.* **331**, 444 (2015)
13. Y.S. Lin, K.J. Ma, C. Hsu, S.W. Feng, Y.C. Cheng, C.C. Liao, C.C. Yang, C.C. Chou, C.M. Lee, J.I. Chyi, *Appl. Phys. Lett.* **77**, 2988 (2000)
14. T. Li, A.M. Fischer, Q.Y. Wei, F.A. Ponce, T. Detchprohm, C. Wetzel, *Appl. Phys. Lett.* **96**, 031906 (2010)
15. M. Feneberg, K. Thonke, *J. Phys. Condens. Matter* **19**, 403201 (2007)
16. K.P. O'Donnell, M.A.D. Maur, A. Di Carlo, K. Lorenz, *Phys. Status Solidi RRL* **6**, 49 (2012)
17. D. Fuhrmann, C. Netzel, U. Rossow, A. Hangleiter, G. Ade, P. Hinze, *Appl. Phys. Lett.* **88**, 071105 (2006)
18. L. Hoffmann, H. Bremers, H. Jönen, U. Rossow, M. Schowalter, T. Mehrrens, A. Rosenauer, A. Hangleiter, *Appl. Phys. Lett.* **102**, 102110 (2013)
19. Z.L. Fang, Applications of surface/interface modification in group-III nitrides, in *Encyclopedia of Semiconductor Nanotechnology, Chapter 4*, vol. 1, ed. by A. Umar (American Scientific Publishers, Valencia, 2012), pp. 1–57
20. H.C. Lin, R.S. Lin, J.I. Chyi, *Appl. Phys. Lett.* **92**, 161113 (2008)
21. M.S. Kumar, J.Y. Park, Y.S. Lee, S.J. Chung, C.H. Hong, E.K. Suh, *Jpn. J. Appl. Phys.* **47**, 839 (2008)
22. Y.B. Tao, Z.Z. Chen, F.F. Zhang, C.Y. Jia, S.L. Qi, T.J. Yu, X.N. Kang, Z.J. Yang, L.P. You, D.P. Yu, G.Y. Zhang, *J. Appl. Phys.* **107**, 103529 (2010)
23. Z.L. Fang, J.Y. Kang, W.Z. Shen, *J. Phys. Chem. C* **112**, 17652 (2008)
24. Z.L. Fang, X.Y. Shen, Z.Y. Wu, T.Y. Zhang, *Phys. Status Solidi A* **212**, 2205 (2015). doi:10.1002/pssa.201532246
25. S.C. Huang, D.S. Wu, P.Y. Wu, S.H. Chan, *IEEE J. Sel. Top. Quantum Electron.* **15**, 1132 (2009)
26. Z. Chen, N. Fichtenbaum, D. Brown, S. Keller, U.K. Mishra, S.P. Denbaars, S. Nakamura, *J. Electron. Mater.* **37**, 546 (2007)
27. S.H. Han, C.Y. Cho, S.J. Lee, T.Y. Park, T.H. Kim, S.H. Park, S.W. Kang, J.W. Kim, Y.C. Kim, S.J. Park, *Appl. Phys. Lett.* **96**, 051113 (2010)
28. Z.L. Fang, J.Y. Kang, W.J. Huang, H.T. Sun, M. Lu, J.F. Kong, W.Z. Shen, *J. Phys. Chem. C* **112**, 4925 (2008)
29. M.S. Kumar, Y.S. Lee, J.Y. Park, S.J. Chung, C.H. Hong, E.K. Suh, *Mater. Chem. Phys.* **113**, 192 (2009)
30. S.M. Ting, J.C. Ramer, D.I. Florescu, V.N. Merai, B.E. Albert, A. Parekh, D.S. Lee, D. Lu, D.V. Christini, L. Liu, E.A. Armour, *J. Appl. Phys.* **94**, 1461 (2003)
31. Z.L. Fang, D.Q. Lin, J.Y. Kang, J.F. Kong, W.Z. Shen, *Nanotechnology* **20**, 235401 (2009)
32. Crosslight Software Inc. (2012) APSYS, Burnaby, Canada. <http://www.crosslight.com>
33. D. Cherns, Y.Q. Wang, R. Liu, F.A. Ponce, *Appl. Phys. Lett.* **81**, 4541 (2002)
34. L. Lahourcade, J. Pernot, A. Wirthmüller, M.P. Chauvat, P. Ruterana, A. Laufer, M. Eickhoff, E. Monroy, *Appl. Phys. Lett.* **95**, 171908 (2009)

35. Z. Liliental-Weber, Y. Chen, S. Ruvimov, J. Washburn, *Phys. Rev. Lett.* **79**, 2835 (1997)
36. J.F. Moulder, W.F. Stickle, P.E. Sobol, K.D. Bomben, *Handbook of X-Ray Photoelectron Spectroscopy: A Reference Book of Standard Spectra for Identification and Interpretation of XPS Data*. Physical Electronics, Minnesota (1995)
37. C.P. Foley, J. Lyngdal, *J. Vac. Sci. Technol. A* **5**, 1708 (1987)
38. D. Gonzalez, J.G. Lozano, M. Herrera, N.D. Browning, S. Ruffenach, O. Briot, R. Garcia, *Phys. Status Solidi C* **1**, 9 (2010)
39. R. Fischer, D. Neuman, H. Zabel, H. Morkoç, C. Choi, N. Otsuka, *Appl. Phys. Lett.* **48**, 1223 (1986)
40. H.M. Wang, J.P. Zhang, C.Q. Chen, Q. Fareed, J.W. Yang, M.A. Khan, *Appl. Phys. Lett.* **81**, 604 (2002)
41. S.R. Xu, Y. Hao, J.C. Zhang, X.W. Zhou, L.A. Yang, J.F. Zhang, H.T. Duan, Z.M. Li, M. Wei, S.G. Hu, Y.R. Cao, Q.W. Zhu, Z.H. Xu, W.P. Gu, *J. Cryst. Growth* **311**, 3622 (2009)
42. S. Vézian, F. Natali, F. Semond, J. Massies, *Phys. Rev. B* **69**, 125329 (2004)
43. U. Jahn, O. Brandt, E. Luna, X. Sun, H. Wang, D.S. Jiang, L.F. Bian, H. Yang, *Phys. Rev. B* **81**, 125314 (2010)